Solid Freeform Fabrication 2022: Proceedings of the 33rd Annual International
Solid Freeform Fabrication Symposium – An Additive Manufacturing Conference
Reviewed Paper

USE OF A FLUID INTERFACE TO REDUCE SUPPORT STRUCTURES IN TOP-DOWN STEREOLITHOGRAPHY

Jenny Wang, Amit Jariwala, David Rosen

Georgia Institute of Technology, Atlanta, GA

Abstract

Stereolithography (SLA) is a vat photopolymerization additive manufacturing process which utilizes ultraviolet (UV) light energy to cure resin layer-by-layer to build parts. The fabrication of overhanging geometry in SLA typically requires sacrificial support structures. Printing supports increases fabrication time and material usage, and their removal prolongs the post-processing and has a detrimental effect on the surface quality of the final part. This study investigates a top-down mask projection SLA system in which a fluid of similar density to the cured resin is used to support the part during fabrication. The buoyant force of the displaced fluid counteracts the gravitational force the part experiences, thus reducing the need for support structures in overhangs. The overall system design is presented, and a first-order analytical model of part deformation resulting from internal stresses and buoyant and gravitational forces is proposed.

1 Introduction and motivation

Additive manufacturing (AM) has proven to be a compelling fabrication solution in a wide variety of usages, as it enables the realization of unique and intricate parts which are beyond the capabilities of conventional manufacturing. In particular, SLA is favored because of its high resolution, smooth surface finish, and isotropy of printed parts. However, due to the sacrificial support structures required to stabilize overhangs, it is still limited in the types of geometries that can be easily made. Printing these support structures increases the print time and wastes valuable material, and the post-processing to remove them is time-consuming and difficult to automate. The removal of supports also lowers the part surface quality.

Past research has addressed these problems in a number of different ways. For fused filament fabrication, a method of using a secondary material for the supports which is then dissolved by a chemical solvent has been demonstrated [1, 2]. A robotic system in which the build platform and the extruder have three degrees of freedom each has proven to be effective in support-free fabrication by tilting the part and printing along different directions as needed [3]. Also, the use of a dynamic build platform composed of vertically movable pins to support overhangs has been validated for both deposition-based and powder-based AM [4]. However, none of these approaches can be applied to SLA. In SLA, studies have been conducted to optimize the geometry and location of support structures, but this does not mitigate the underlying need for the part to be supported during fabrication [5-7].

The present research involves the design of a novel stereolithography process, Fluid Interface Supported Printing (FISP), which eliminates or reduces the necessity of supports. This process uses a fluid immiscible with the liquid resin and similar in density to the cured part to support the part as it is fabricated. Use of fluid interfaces in SLA printing has been previously investigated. Bhanvadia et al. utilized a fluorinated oil to create an oxygen dead zone between the cured part and the build window [8]. Walker et al. devised a similar process with a mobile fluid interface to mitigate thermal buildup in addition to preventing adhesion to the build window [9]. A patent by Carbon details a bottom-up SLA system in which the resin rests atop an immiscible fluid, enabling continuous fabrication [10]. The FISP system differs from this in that the cured geometry is lowered and retained in the immiscible support fluid rather than being drawn up out of it. In FISP, the purpose of the support fluid is to provide a buoyancy force to counteract the gravitational force the cured geometry experiences. General proof of concept for FISP has been demonstrated by Mulka et al. [11, 12]. Figure 1 shows a comparison between an unsupported bridge fabricated with a commercial SLA printer and the same part fabricated with FISP. It can be seen that the FISP print is successful, while the commercial print exhibits significant deformation in the unsupported region. Furthermore, Figure 2 illustrates the capability of FISP to fabricate a horizontal overhang and a part inclined 15° from horizontal. This confirms the feasibility of using a fluid support bath in SLA to print overhanging geometries without support structures.

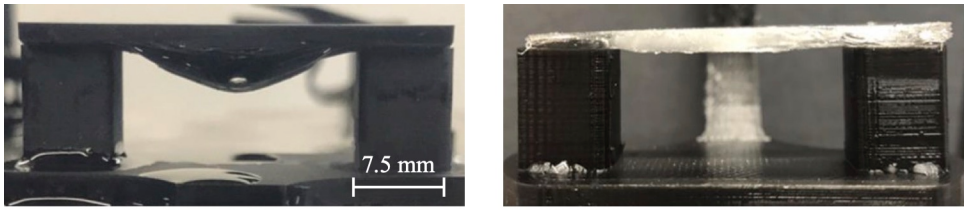

Figure 1: Side views of unsupported bridge geometry – (a) printed with commercial SLA printer, (b) printed with FISP [12]

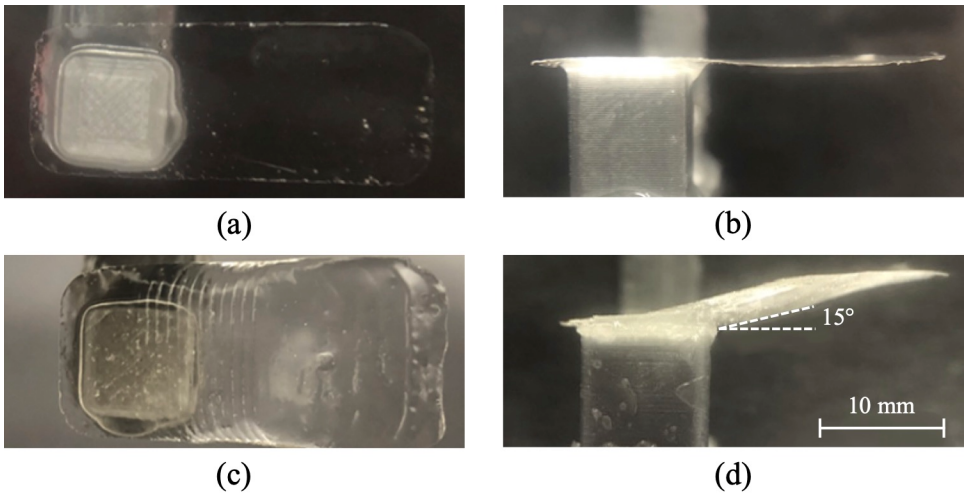

Figure 2: Parts fabricated with the FISP system – (a) horizontal top view, (b) horizontal side view, (c) 15° from horizontal top view, (d) 15° from horizontal side view [11]

In this paper, a more robust system design is presented along with a thorough characterization of the forces acting on the cured part. A basic analytical model of part deformation due to these forces is established. Negating the need for support structures allows for near-infinite design freedom in the creation of complex geometries with overhangs. Additionally, the manufacture of these parts can be made simpler, faster, and more efficient. In this manner, the present research expands the possibilities and applications of the vast field of additive manufacturing.

2 Methods

2.1 Fluid interface supported printing system design

FISP is a top-down mask projection SLA process. Figure 3 shows a schematic of the system. An Acer X113P digital light processing (DLP) projector is used as the UV light source. The projector also functions as a dynamic mask by projecting the shapes to be cured with a black background. The UV intensity can be controlled by adjusting the grayscale value of the projected shapes. A convex lens is used to resize the image from the projector and focus it at a closer distance, and a 45° mirror directs it downward to the fluid container. The fluid container is filled with the support fluid with a thin layer of photopolymer resin on top. The print bed is fixed to an ASI MS-2000 translation stage which enables it to move in the vertical direction. After each layer is cured, the print bed moves down, submerging the part in the support fluid.

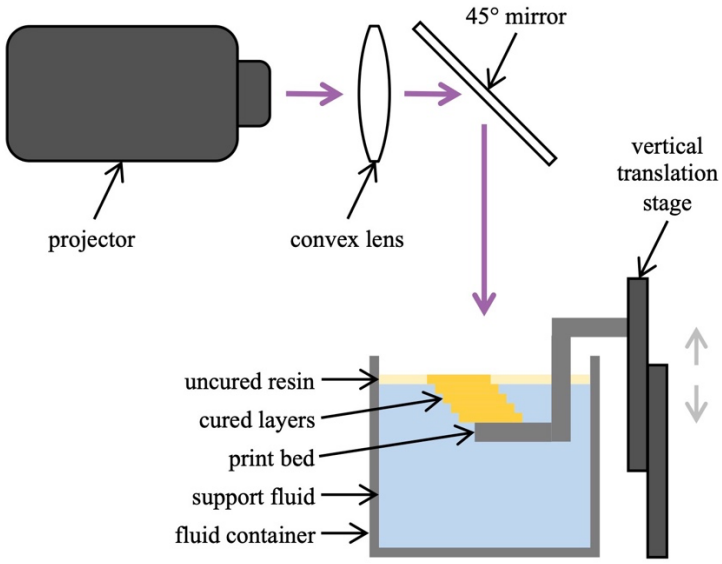

Figure 3: FISP system schematic

2.2 Materials selection

A commercial acrylate UV resin supplied by Anycubic was used in the prints. Material properties of the resin are given in Table 1. The resin was chosen for its low viscosity and spreading behavior, as it must be able to easily spread across the surface of the support fluid and refill the space vacated by the cured geometry as the print bed moves down.

Table 1: Material properties of Anycubic UV resin [13]

Property	Value
Curing wavelength	405 nm
Viscosity	552 mPa·s
Volumetric shrinkage	7.1 %
Tensile strength	23.4 MPa
Liquid density	1.100 g/cm^3
Solid density	1.184 g/cm^3

The support fluid must be immiscible with the liquid resin and similar in density to the cured resin. Additionally, it must be chemically unreactive with the resin and UV light. Considering these characteristics, saline solution was chosen as the support fluid. The density of the saline can be finely tuned by adding a deliberate amount of salt.

2.3 Controls automation and integration

The parts of the system that require controls are the projector and the translation stage which moves the print bed. The projector can be programmed with MATLAB to display a series of timed images, with each image corresponding to a layer. Between projections, there is a delay to allow time for the print bed to be moved down in preparation for the next layer to be cured. The translation stage can either be moved manually or controlled with the ASI Console or MATLAB. Given the images to be projected and their corresponding exposure times, the layer thickness, and the print bed movement speed, the fabrication of a part can be fully automated with a MATLAB script.

3 Cured geometry deflection modeling

3.1 Forces acting on the fabricated part

The free body diagrams for curing an unsupported overhang in the FISP system are given in Figure 4. Figure 4a and Figure 4b show the forces acting on the current layer being cured and the previously cured part, respectively. There are vertical forces due to the difference in density of the materials, i.e. the buoyant and gravitational forces for the layer and the previously cured part, which are denoted in the figure as $F_{\rho,layer}$ and $F_{\rho,part}$. The internal stresses of the layer and previously cured part, $F_{in,layer}$ and $F_{in,part}$, cause them to shrink in the lateral directions. The adhesion between the layer and the previously cured part, $F_{interface}$, opposes this motion. There is also a surface tension

force, F_γ, at the interface of the resin and the support fluid along the perimeter of the part. Additionally, when the print bed is moved down, a drag force, F_d, is introduced.

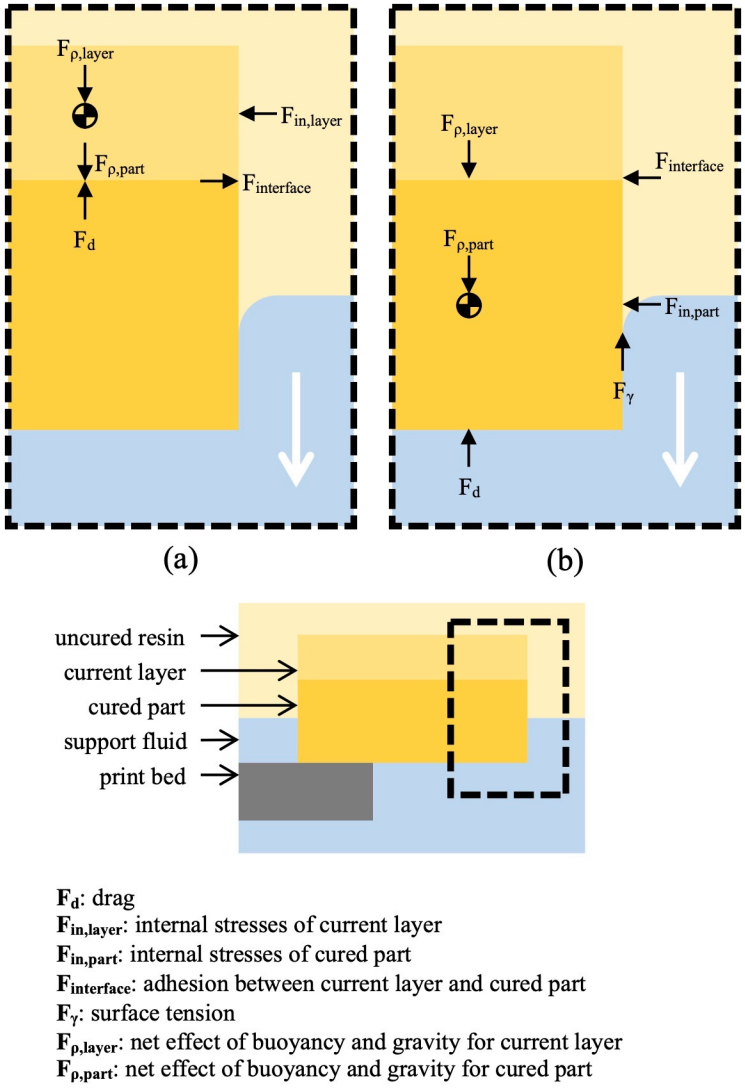

Figure 4: Free body diagrams – (a) current layer being cured, (b) previously cured part

By moving the print bed at slow speeds, F_d can be assumed to be negligible. Additionally, the value of F_γ is typically very small for low viscosity resins. Mulka et al. [11] have confirmed that the effect of surface tension in printing macro-scale geometry with FISP is trivial. Thus, the most significant forces are F_{in} and F_ρ. The following sections discuss modeling the effect of these forces in detail.

3.2 Deflection due to polymerization strains

The internal stresses of the part are caused by thermal effects and polymerization shrinkage. During polymerization, the part shrinks as the monomer is cross-linked into a tighter

molecular structure. Additionally, the change in temperature due to the heat released from the exothermic reaction causes the part to expand. After the reaction is complete, the part contracts as heat is dissipated. Nonuniform shrinkage of the material leads the part to deform. In this study, small layer thicknesses are used, and the relatively large volume of support fluid acts to conduct heat away from the reaction zone. Therefore, the thermal volume changes are expected to be minimal, and only polymerization shrinkage is considered.

To model the deflection, the part is regarded as a number of discrete layers, each with a constant average conversion value. From the conversion, the specific volume of each layer can be calculated using Equation 1, where v_m and v_p are the specific volumes of the monomer and the fully cured solid polymer, and X is the conversion. Then, the strain can be calculated using Equation 2.

$$v = (1 - X)v_m + Xv_p \tag{1}$$

$$\varepsilon = \left(\frac{v}{v_m}\right)^{1/3} - 1 \tag{2}$$

The deformation due to the different strains between layers can be estimated using the multi-metallic strip model, which is illustrated in Figure 5. The radius of curvature for a composite strip of n layers is given by Equation 3, where ij denotes all two-number combinations of layers 1 to n, Y is the Young's modulus, and h is the layer thickness [14].

$$R = \frac{\sum a_{ij} + 4cd}{2\sum b_{ij}} \tag{3}$$

$$a_{ij} = Y_i Y_j h_i h_j \left(h_i + 2\sum_{k=i+1}^{j-1} h_k + h_j\right)^2 \tag{3a}$$

$$b_{ij} = Y_i Y_j h_i h_j \left(h_i + 2\sum_{k=i+1}^{j-1} h_k + h_j\right)(\varepsilon_j - \varepsilon_i) \tag{3b}$$

$$c = \sum_{k=1}^{n} \left(\frac{Y_k h_k^3}{12}\right) \tag{3c}$$

$$d = \sum_{k=1}^{n} (Y_k h_k) \tag{3d}$$

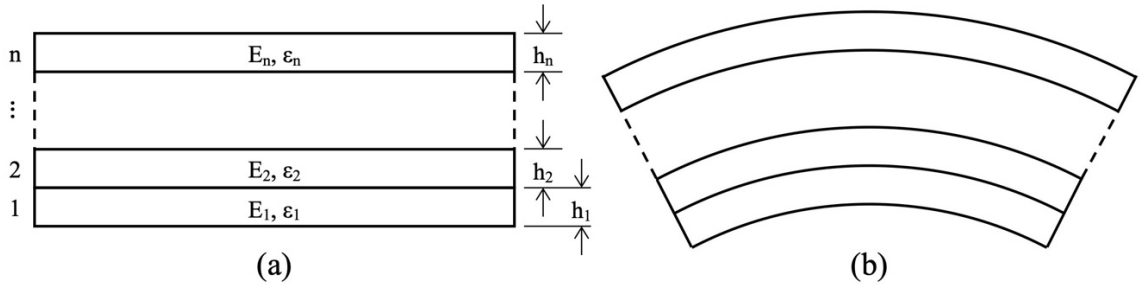

Figure 5: Multi-metallic strip model – (a) undeformed, (b) deformed due to strains

3.3 Deflection due to gravitational and buoyant forces

F_ρ can be calculated for a part submerged in the support fluid using Equation 4, where b, H, and L are the width, thickness and length of the part, g is the acceleration of gravity, and ρ_f and ρ_s are the densities of the support fluid and the cured solid part. If the part is not entirely submerged in the support fluid, then the force must be considered separately for the portion in the support fluid and the portion in the resin layer, as shown in Equation 5, where ρ_r is the density of the liquid resin, H_r is the thickness of the portion submerged in resin, and H_f is the thickness of the portion submerged in support fluid.

$$F_\rho = bHLg(\rho_f - \rho_s) \tag{4}$$

$$F_\rho = bLg(H_r(\rho_r - \rho_s) + H_f(\rho_f - \rho_s)) \tag{5}$$

F_ρ acts as a uniformly distributed load on a cantilever beam, as shown in Figure 6. The deflection along the beam is defined by Equation 6, where q is the load per length, Y is the Young's modulus, and I is the area moment of inertia.

$$\delta(x) = q\left(\frac{x^2}{24YI}\right)(6L^2 - 4Lx + x^2) \tag{6}$$

The area moment of inertia for a composite beam is calculated using the transformed area method. The equivalent width for each layer is given by Equation 7, where Y_0 is Young's modulus of the chosen reference layer. The location of the neutral axis can be determined using Equation 8, where y is the location of the neutral axis for the given layer. The area moment of inertia is then calculated using Equation 9.

$$b_{eq,i} = \frac{Y_i}{Y_0} b_i \tag{7}$$

$$\bar{y} = \frac{\sum(y_i b_{eq,i} h_i)}{\sum(b_{eq,i} h_i)} \tag{8}$$

$$I = \sum\left(\frac{1}{12} b_{eq,i} h_i^3 + b_{eq,i} h_i (y_i - \bar{y})^2\right) \tag{9}$$

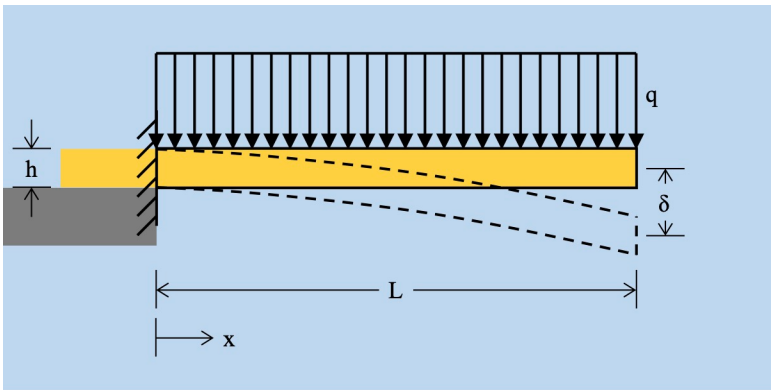

Figure 6: Distributed load on cantilever beam

3.4 Simulation of deflection in multi-layer cantilever beams

The conversion at a vertical location in the resin can be determined by Equation 10, where z is the vertical depth into the resin, K is the polymerization propagation rate, I_0 is the exposure intensity at the surface of the resin, t is the exposure time, and D_p is the resin penetration depth [15].

$$X(z) = 1 - \exp\left(-KI_0 t \exp\left(-\frac{z}{D_p}\right)\right) \tag{10}$$

For this study, values of D_p and the critical energy, E_c, were determined experimentally. In literature, common acrylate resins are reported to have a critical conversion value of approximately 12 % [16, 17]. Therefore, the value for K was chosen such that at the critical time of E_c/I_0, the conversion equaled 12 % at the surface of the resin where the z depth is zero. The shrinkage strain was then calculated using Equations 1 and 2. The Young's modulus for the fully cured resin was experimentally determined to be approximately 270 MPa. It was assumed that the Young's modulus varied linearly between 0 and 135 MPa for conversion values of 0 to 12 %, and 135 and 270 MPa for conversion values of 12 to 100 %. The constants used in these calculations are given in Table 2.

Table 2: Constants used in polymerization strain calculation

Constant	Value
Surface exposure intensity (I_0)	26.95 W/m^2
Critical energy (E_c)	430.9 J/m^2
Penetration depth (D_p)	0.6132 mm
Polymerization propagation rate (K)	0.0002967
Young's modulus (Y)	270 MPa

The deflection due to polymerization shrinkage was simulated in multi-layer cantilever beams using the multi-metallic strip model described in section 3.1. To account for the conversion gradient within the layers, each layer was approximated as several discrete sub-layers with constant conversion values. Additionally, the deflection due to gravitational and buoyant forces was calculated as described in section 3.2. In the following analysis, the layers are numbered from the bottom up, as in the direction of fabrication, and the sub-layers within each layer are numbered from the top down, as in the direction of irradiation.

4 Results and discussion

4.1 Deflection due to polymerization strains

The fabrication of a 20-layer part was simulated with 10 sub-layers per layer, a layer thickness of 50 μm, length of 20 mm, width of 5 mm, and exposure time per layer of 20 s. Table 3 lists the percent conversion of each sub-layer of the first and bottommost layer after the first 10

exposures. The rest of the layers follow the same pattern, i.e., the conversion values for layer 2 after the second exposure are the same as those for layer 1 after the first exposure, and so on. It can be seen that the conversion reaches 100 % and ceases to increase at the 10th exposure. In Figure 7, the maximum vertical deflection at the free end of the beam relative to the beam length and the maximum conversion within the part are plotted against the exposure number. Plotting normalized deflection nondimensionalizes the results so they are more generally applicable. As expected, the maximum deflection is positive after the first layer is cured due to the conversion gradient. The top of the layer has a higher conversion, and therefore, shrinkage, than the bottom, which causes the part to curl upward. Subsequently, the deflection lessens with more exposures as more layers are cured, and the differences in polymerization strains between adjacent layers decrease. Then there is a sharp increase in deflection, which coincides with the saturation of the conversion. This occurs because of the large difference in strains between the bottom of the part, which is no longer shrinking, and the layers above, which still shrink significantly. However, as the exposures continue and more layers become saturated, this effect is mitigated, and the deflection is reduced. Figure 8 plots the maximum deflection after each exposure for per-layer exposure times between 20 and 30 s. This demonstrates that longer exposure times cause larger deflections due to greater differences in conversion between layers.

Table 3: Percent conversion of each sub-layer of the first layer after the first 10 exposures

	Exp. 1	**Exp. 2**	**Exp. 3**	**Exp. 4**	**Exp. 5**	**Exp. 6**	**Exp. 7**	**Exp. 8**	**Exp. 9**	**Exp. 10**
Sub-layer 1	14.78	28.48	41.19	52.96	63.86	73.95	83.29	91.93	99.92	100
Sub-layer 2	14.67	28.27	40.88	52.56	63.37	73.39	82.65	91.23	99.16	100
Sub-layer 3	14.56	28.06	40.57	52.16	62.89	72.83	82.02	90.53	98.40	100
Sub-layer 4	14.45	27.85	40.26	51.76	62.42	72.28	81.40	89.84	97.65	100
Sub-layer 5	14.34	27.64	39.96	51.37	61.94	71.73	80.78	89.16	96.90	100
Sub-layer 6	14.23	27.43	39.66	50.98	61.47	71.18	80.16	88.47	96.16	100
Sub-layer 7	14.13	27.22	39.36	50.60	61.00	70.64	79.55	87.80	95.42	100
Sub-layer 8	14.02	27.02	39.06	50.21	60.54	70.10	78.95	87.13	94.69	100
Sub-layer 9	13.91	26.81	38.76	49.83	60.08	69.57	78.34	86.46	93.97	100
Sub-layer 10	13.81	26.61	38.47	49.45	59.62	69.04	77.74	85.80	93.25	100

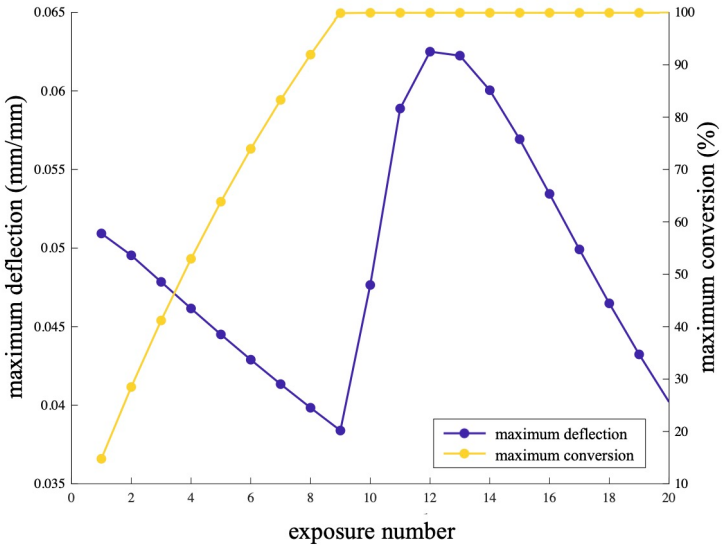

Figure 7: Maximum deflection and maximum conversion after each exposure

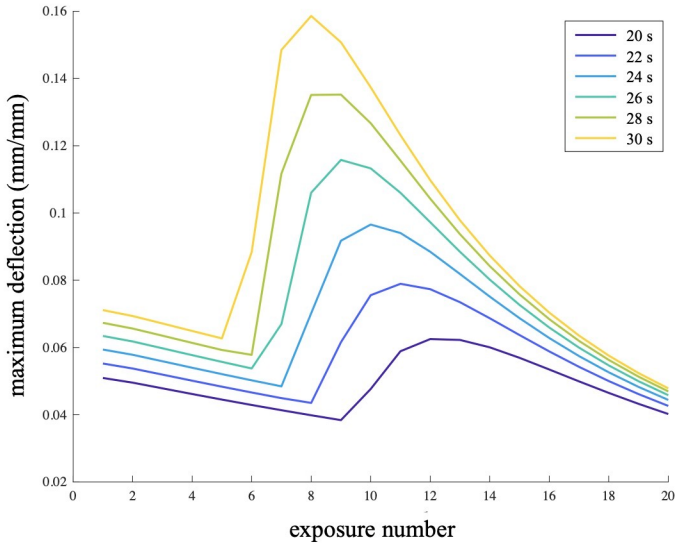

Figure 8: maximum deflection after each exposure for different exposure times

4.2 Deflection due to gravitational and buoyant forces

The deflection due to material density differences, i.e., the net effect of the gravitational and buoyant forces, was investigated for the same part described in the previous section. Figure 9a plots the maximum deflection due to gravity without a buoyant force to counteract it, and the maximum deflection of the part submerged in uncured resin. Figure 9b plots the maximum deflection of the part submerged in uncured resin compared with different concentrations of saline. The deflection is greatest at the beginning, and lessens as more layers are added and the thickness and stiffness of the part increase. While the deflection after a number of exposures is very small

in the case of submergence in resin and saline, a significant initial negative deflection can be very detrimental to the part quality, as it causes delamination between layers. However, these results demonstrate that with the optimal density support fluid, the effect of the gravitational and buoyant forces can be nearly eliminated.

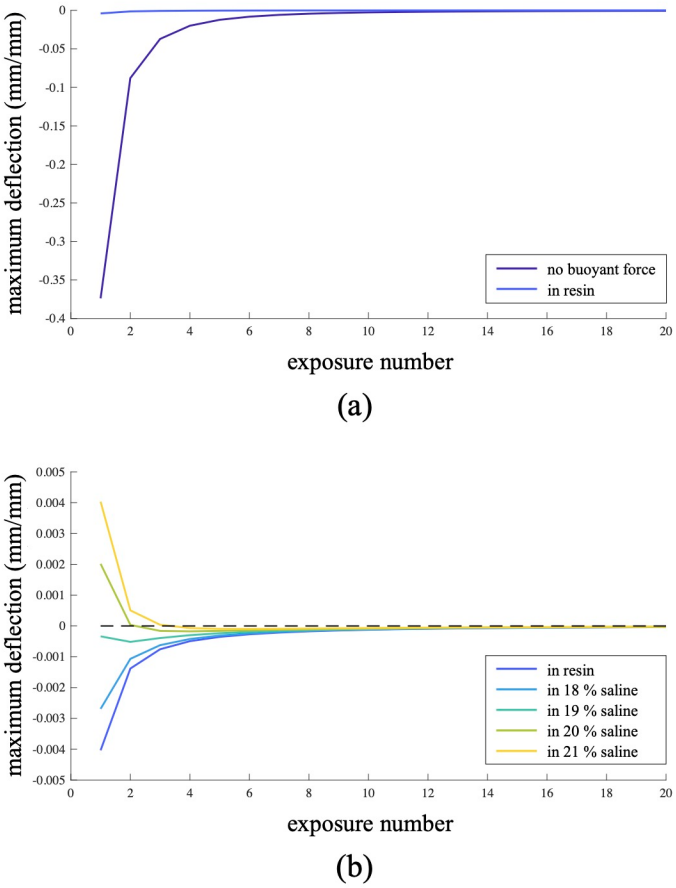

Figure 9: Deflection due to density differences – (a) without buoyant force and with buoyant force of resin, (b) with buoyant force of resin and saline

4.3 Summary and discussion of results

The models presented in this paper succeed in capturing the general qualitative trends of FISP curing which are consistent with experimental observations [11, 12]. However, due to the modeling assumptions made, the accuracy of the quantitative results is likely not high. The main limitation of this work is that it evaluates the FISP process as a series of discrete, independent timesteps. However, in reality, the process is intricately time-dependent. Polymerization occurs continuously, and the conversion throughout the part changes at different rates. A layer only begins to adhere to the previous one and deform with it after a certain conversion is reached. Additionally, the deformation of each layer affects the fabrication of the subsequent layers. While the present research does not account for these effects, it lays the groundwork for more sophisticated

computational models capable of predicting part deformation at a higher degree of accuracy to be created.

5 Conclusion and future work

The present research provides an analytical model of deformation in parts fabricated with FISP. Two main causes of deformation were identified—polymerization strains and the net effect of gravity and buoyancy. To predict the deformation of a cantilever beam, the cured part was approximated as discrete layers with constant properties. Deformation due to polymerization strains was modeled using the multi-metallic strip model, and the gravitational and buoyant forces were modeled as a uniformly distributed load on a composite cantilever beam. The results showed expected qualitative trends and confirmed that use of a support fluid can minimize the effect of gravity on the cured part.

In terms of future work, a more thorough model will be developed. To accurately predict the deformation of parts manufactured with FISP, a dynamic, continuous model is needed. Once such a model is established for multi-layer cantilever beams, it will be expanded and applied to more complex geometries.

References

1. Priedeman, W.R., Brosch, A.L., *Soluble material and process for three-dimensional modeling*. 2004, Stratasys Inc.: United States.
2. Chueca de Bruijn, A., G. Gómez-Gras, and M.A. Pérez, *Mechanical study on the impact of an effective solvent support-removal methodology for FDM Ultem 9085 parts.* Polymer Testing, 2020. **85**: p. 106433.
3. Wu, C., et al. *RoboFDM: A robotic system for support-free fabrication using FDM*. in *2017 IEEE International Conference on Robotics and Automation (ICRA)*. 2017.
4. Yigit, I.E. and I. Lazoglu. *Dynamic Build Bed for Additive Manufacturing*. in *2019 International Solid Freeform Fabrication Symposium*. 2019. University of Texas at Austin.
5. Wei, X., et al., *Toward Support-Free 3D Printing: A Skeletal Approach for Partitioning Models.* IEEE Transactions on Visualization and Computer Graphics, 2018. **24**: p. 2799-2812.
6. Zhang, N., et al., *Local Barycenter Based Efficient Tree-Support Generation for 3D Printing.* Computer-Aided Design, 2019. **115**.
7. Jiang, J., X. Xu, and J. Stringer, *Support Structures for Additive Manufacturing: A Review.* Journal of Manufacturing and Materials Processing, 2018. **2**(4).
8. Bhanvadia, A.A., et al., *High-resolution stereolithography using a static liquid constrained interface.* Communications Materials, 2021. **2**(1): p. 1-7.
9. Walker, D.A., J.L. Hedrick, and C.A. Mirkin, *Rapid, large-volume, thermally controlled 3D printing using a mobile liquid interface.* Science, 2019. **366**(6463): p. 360-364.
10. Robeson, L.M., et al., *Continuous three dimensional fabrication from immiscible liquids*. 2019, Google Patents.

11. Mulka, N., et al. *Static Liquid Interface to Reduce Support Structure Necessity in Top-Down Stereolithography*. in *2021 International Solid Freeform Fabrication Symposium*. 2021. University of Texas at Austin.
12. Mulka, N., *Fluid interface supported printing for three-dimensional object fabrication*, in *Mechancial Engineering*. 2022, Georgia Institute of Technology.
13. Anycubic, *ANYCUBIC 3D Printer Resin, 405nm SLA UV-Curing Resin, High Precision & Rapid Photopolymer for LCD/DLP/SLA 3D Printing*. 2018.
14. Vasudevan, M. and W. Johnson, *On multi-metal thermostats.* Applied Scientific Research, Section B, 1961. **9**(6): p. 420-430.
15. Wu, X., et al., *Modeling and visualization of layered curing conversion profile in ceramic mask projection stereolithography process.* Ceramics International, 2020. **46**(16, Part A): p. 25750-25757.
16. Boddapati, A., *Modeling cure depth during photopolymerization of multifunctional acrylates*. 2010, Georgia Institute of Technology.
17. Kim, W.G. and J.Y. Lee, *Cure kinetics of methacrylate-type resin that include cyclohexane moiety.* Polymer, 2003. **44**(20): p. 6303-6309.